



CFD verification and validation of green sea loads

Inno Gatin^a, Vuko Vukčević^a, Hrvoje Jasak^{a,b,*}, Jeonghwa Seo^c, Shin Hyung Rhee^c

^a University of Zagreb, Faculty of Mechanical Engineering and Naval Architecture, Ivana Lučića 5, Zagreb, Croatia

^b Wikki Ltd, 459 Southbank House, SE1 7SJ, London, United Kingdom

^c Research Institute of Marine Systems Engineering, Seoul National University, Gwanak-ro 1, Gwanak-gu, Seoul, 08826, South Korea

ARTICLE INFO

Keywords:

Green sea loads
Regular waves
CFD
Naval Hydro pack
VOF

ABSTRACT

An extensive verification and validation for green sea load simulations is presented. The calculations are performed using the Naval Hydro pack, a library based on foam–extend, which is an open source Computational Fluid Dynamics software. The geometric Volume of Fluid method is used for interface advection, while the Ghost Fluid Method is employed to discretise the free surface boundary conditions at the interface. Pressure measured at the deck of a fixed structure is compared to experimental data for nine regular waves. Verification is performed using four refinement levels in order to reliably assess numerical uncertainties. A detailed uncertainty analysis comprises both numerical and experimental data. Comparable uncertainties are exhibited in simulations and experiments, with good agreement of results.

1. Introduction

In the field of offshore and marine engineering, wave loading poses a wide range of different challenges which are important in the design process. One of the more difficult wave–related problems to describe and reliably estimate is the green sea load. Green sea, or water on deck, is a consequence of a highly nonlinear interaction between the floating structure and the free surface waves, which comprise incident, diffracted and radiated waves. The complex origin of the phenomenon renders the prediction of green sea occurrence challenging. Apart from that, violent two phase flow develops once the water is on the deck, which is difficult to predict via simplified flow theories. Green sea effect cause both local and global structural loads which can endanger the structural integrity, and therefore must be taken into account in the design process.

Given the complexity of the problem, experimental and numerical means are currently utilised to calculate green sea loads. According to Tamarel et al. (Temarel et al., 2016), both experimental and numerical methods available today are not mature to reliably assess green sea loads. Hence, further research is needed to establish confidence in both fields. As a result, a wide variety of methods have been developed and applied in recent years. Greco et al. (2012) used the numerical solver developed by Greco and Lugni (2012) to calculate wave loads on a patrol ship, including green sea loads with comparison to experiments. Lu et al. (2012) developed a time domain numerical method based on Finite

Volume (FV) method used for green sea load simulations. Xu (2013) used Smoothed Particle Hydrodynamics to simulate breaking waves plunging onto a deck. Zhao et al. (2014) studied the influence of structure motion on the pressure loads due to green sea effects using a FV based method. Kim et al. (2013) used a linear method for assessing the ship motion, and a nonlinear viscous method to calculate green sea loads on a container vessel. Ruggeri et al. (2013) used WAMIT software based on the potential flow model and a viscous FV code StarCCM+ to devise guidelines for green sea load calculations. Joga et al. (2014) compared two viscous FV codes with experimental results of water ingress into open ship holds during green sea events. Pakozdi et al. (2014) coupled a potential flow based method and a viscous model to conduct simulations of green sea events. Zhu et al. (2009) conducted numerical simulations of green sea events for a Floating Production, Storage and Offloading (FPSO) vessel.

In this work, a detailed validation study of green sea loads on a static structure is conducted. Experimental results published by Lee et al. (2012) are used for the comparison. Nine regular wave cases are investigated, including the uncertainty analysis of numerical and experimental results. Naval Hydro software pack is used for numerical simulations, which is an extension of the collocated FV based CFD open source software foam–extend (Weller et al., 1998; Jasak, 2009). The Naval Hydro package is specialised for viscous, two phase, large scale flows. Nonlinear stream function regular wave theory by Rienecker and Fenton (1981) is used for wave generation. The potential wave flow and CFD are coupled

* Corresponding author. University of Zagreb, Faculty of Mechanical Engineering and Naval Architecture, Ivana Lučića 5, Zagreb, Croatia.

E-mail addresses: inno.gatin@fsb.hr (I. Gatin), vuko.vukcevic@fsb.hr (V. Vukčević), h.jasak@wikki.co.uk, hrvoje.jasak@fsb.hr (H. Jasak), thamjang@snu.ac.kr (J. Seo), shr@snu.ac.kr (S.H. Rhee).

<https://doi.org/10.1016/j.oceaneng.2017.10.026>

Received 5 June 2017; Received in revised form 29 August 2017; Accepted 16 October 2017

in a one-way fashion using implicit relaxation zones (Jasak et al., 2015) by imposing the wave solution at the boundaries of the domain and gradually transitioning to the nonlinear CFD solution towards the middle of the domain. The interface is captured using the Volume of Fluid (VOF) method where a novel geometric approach developed by Roenby et al. (2016) is employed, called isoAdvector. Free surface boundary conditions are discretised using the Ghost Fluid Method (GFM) (Vukčević, 2016), providing an infinitesimally sharp pressure and density gradient distribution at the interface.

The aim of this paper is to assess the accuracy and feasibility of a modern naval hydrodynamics CFD software for predicting green sea loads. In order to reduce the possible sources of error to a minimum, a simple static geometry is analysed with publicly available experimental results (Lee et al., 2012). Since numerical simulations of wave induced motions and loads have been validated using the Naval Hydro package in the past (Vukčević, 2016; Vukčević et al., 2015, 2016; Jasak et al., 2014), green sea load validation is the missing piece for conducting complete numerical simulations with moving bodies where green sea loads are calculated.

This paper is organised as follows: in the second chapter the numerical method is outlined. The third chapter gives basic information about experimental measurements that are used for comparison. In the fourth chapter the numerical simulations of green sea loads are described in detail, including the simulation set-up, uncertainty analysis procedure and comparison of the results with the experiments. Finally, a brief conclusion is given.

2. Numerical model

In this section the numerical model used in this work is presented. Governing equations describing two-phase, incompressible and viscous flow are:

$$\nabla \cdot \mathbf{u} = 0, \quad (1)$$

$$\frac{d\mathbf{u}}{dt} + \nabla \cdot (\mathbf{u}\mathbf{u}) - \nabla \cdot (\nu \nabla \mathbf{u}) = -\frac{1}{\rho} \nabla p_d, \quad (2)$$

where \mathbf{u} denotes the velocity field, ν stands for the kinematic viscosity of the corresponding phase, ρ is the density, while p_d stands for dynamic pressure:

$$p_d = p - \rho \mathbf{g} \cdot \mathbf{x}. \quad (3)$$

Here, p is the absolute pressure, \mathbf{g} is the gravitational acceleration, while \mathbf{x} denotes the radii vector. Note that the momentum equation has been divided through by the density, assuming a two-phase free surface system of incompressible immiscible fluids. Eq. (1) and Eq. (2) are discretised in collocated FV fashion yielding the pressure and momentum equation (Vukčević et al., 2017), respectively. The equations are solved implicitly. Eq. (2) is valid for both phases, where the discontinuity of dynamic pressure and density at the interface is taken into account with the GFM (Vukčević, 2016; Vukčević et al., 2017). The dynamic pressure and density jump conditions are a consequence of normal stress balance at the free surface. The tangential stress balance is modelled approximately, while the surface tension is neglected. The two jump conditions arising from the normal stress balance are:

$$p_d^- - p_d^+ = -(\rho^- + \rho^+) \mathbf{g} \cdot \mathbf{x}, \quad (4)$$

$$\frac{1}{\rho^-} \nabla p_d^- - \frac{1}{\rho^+} \nabla p_d^+ = 0. \quad (5)$$

Superscripts “+” and “-” denote the water and air phase, respectively. Eq. (4) states that the jump of dynamic pressure across the interface is proportional to the jump in density, while Eq. (5) states that the jump of

specific dynamic pressure gradient is zero. The jump conditions are introduced into the discretisation via specialised discretisation schemes, ensuring that Eq. (4) and Eq. (5) are satisfied. The reader is referred to Vukčević et al. (2017) for details.

In order to advect the interface, a geometric VOF method called isoAdvector (Roenby et al., 2016) is used. Standard advection equation is used in order to transport the volume fraction variable α :

$$\frac{\partial \alpha}{\partial t} + \nabla \cdot (\alpha \mathbf{u}) = 0. \quad (6)$$

Written for a finite control volume P , and discretised in time using the first order accurate Euler method, Eq. (6) states:

$$\int_{V_P} \alpha_P(t + \Delta t) - \alpha_P(t) dV = - \int_t^{t+\Delta t} \oint_{S_P} \alpha \mathbf{n} \mathbf{u} dS d\tau, \quad (7)$$

where V_P is the volume of the control volume P , S_P is the closed boundary surface of the control volume, \mathbf{n} is the unit normal vector of the boundary surface, while τ denotes the time integration variable. For a surface boundary discretised with a finite number of faces, the closed surface integral is replaced with a sum of surface integrals across the faces:

$$V_P(\alpha_P(t + \Delta t) - \alpha_P(t)) = - \sum_f \int_t^{t+\Delta t} \int_{S_f} \alpha \mathbf{n}_f \mathbf{u} dS_f d\tau, \quad (8)$$

where f denotes the face index. The volume integral of the temporal term is discretised assuming a second order accurate FV method (Jasak, 1996). Instead of evaluating the temporal and surface integrals in Eq. (8) by employing conventional discretisation schemes, in the isoAdvector method they are integrated explicitly directly from the information about the moving iso-surface of the volume fraction, representing the interface, through a polyhedral cell. In this way, sub-grid resolution is achieved for interface advection. This results in a sharp interface and bounded volume fraction field. The reader is directed to (Roenby et al., 2016) for more details on the isoAdvector method.

2.1. Wave modelling

Regular waves are imposed into the CFD domain via implicit relaxation zones (Jasak et al., 2015). Relaxation zones are regions in the computational domain where the theoretical wave solution is imposed by smoothly transitioning to the calculated CFD solution. The same method is used to dampen the waves at the outlet, where the CFD solution is gradually replaced by the imposed solution, the incident wave in this case. A stream function wave model (Rienecker and Fenton, 1981) is used which is fully nonlinear, permitting a shorter CFD domain since the wave nonlinearities are resolved outside of the CFD domain.

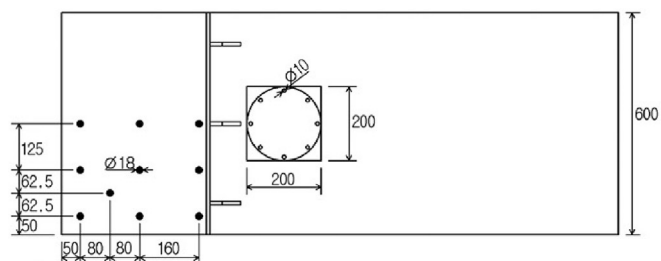
3. Green sea experiments

The experimental tests were performed in the towing tank of Seoul National University, with the details and results published in (Lee et al., 2012). A simplified model of a FPSO vessel is used, where three different bow shape configurations are tested. The computations in this work are performed for one of the geometries, called Rect0 in the original paper (Lee et al., 2012). The structure is static in order to reduce the number of possible sources of error when comparing the results. Ten pressure gauges are positioned at the deck of the model. The geometry of the model and position of pressure gauges are shown in Fig. 1. A vertical wall is positioned at the deck to simulate the breakwater. Pressure data is measured for nine incident wave cases, with wave parameters shown in Table 1. Pressure gauges are labelled as indicated in Fig. 1 in a separate figure for clarity.

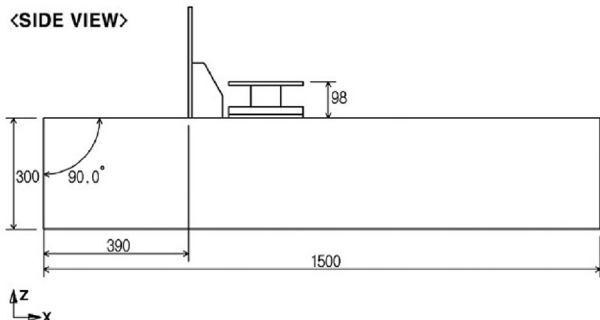
In (Lee et al., 2012) detailed experimental results are presented for pressure peaks of individual gauges. The reported values are average

RECT0

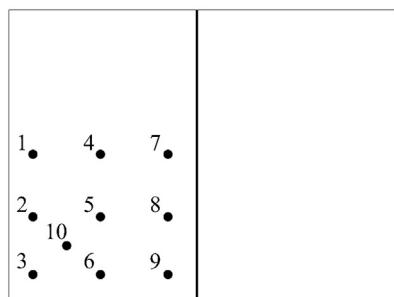
<TOP VIEW>



<SIDE VIEW>



(a)



(b)

Fig. 1. Geometry of the FPSO model: a) model dimensions and pressure gauge positions (pressure gauges are indicated with black dots) (Lee et al., 2012), b) schematic of pressure gauges arrangement with labels.

pressure peaks over 35 incident wave periods. Maximum and minimum values of peaks are also reported, enabling the assessment of periodic uncertainty. However, from the elastic structural response point of view, the integral of force (i.e. pressure) is more relevant than extremely short force peaks. For that reason, additional post-processing of raw

Table 1
Incident wave parameters.

Wave ID	λ , m	a , m	ka
1	2.25	0.04500	0.126
2	2.25	0.05625	0.157
3	2.25	0.06750	0.188
4	3.00	0.06000	0.126
5	3.00	0.07500	0.157
6	3.00	0.09000	0.188
7	3.75	0.07500	0.126
8	3.75	0.09375	0.157
9	3.75	0.11250	0.188

experimental data is performed in order to establish the average pressure time integral in one wave period, as well as maximum and minimum values.

The total experimental uncertainties are calculated as the superposition of measuring uncertainties: bias and precision limit of pressure gauges; and of periodic uncertainty of the pressure peak or pressure integral in time. The bias and precision limit are stated in (Lee et al., 2012). Periodic uncertainty is calculated as:

$$U_{EP} = \frac{\phi_{\max} - \phi_{\min}}{N_E}, \tag{9}$$

where ϕ denotes an arbitrary measured item in one wave period, such as pressure peak or pressure integral, while N_E stands for the number of periods included in the analysis. ϕ_{\max} and ϕ_{\min} are the maximum and minimum values measured during N_E periods. Total experimental uncertainty is then:

$$U_{ET} = \sqrt{U_{EM}^2 + U_{EP}^2}, \tag{10}$$

where U_{EM} stands for measuring uncertainties comprised of bias and precision limit of the pressure gauges.

4. Green sea simulations

In this section the simulations of green sea loading are presented. First, the simulation setup is described in detail, followed by a brief description of the numerical uncertainty analysis used in this work. Second, the results are shown, where first a sensitivity study is performed regarding domain size, in order to justify the reduction of the domain size described below. Next, the results are compared to experimental data, followed by a short discussion. Finally, another sensitivity study is performed regarding the interface capturing method, where the isoAdvect method is compared to the conventional algebraic VOF method (Rusche, 2002).

4.1. Simulation setup

Simulations have been performed for all wave cases for geometry Rect0 with vertical stem. Four grids are used for each wave case in order to establish the numerical uncertainty, while the results from the finest grid are used as reference results for the comparison. Fig. 2 shows the computational domain for wave 4 as an example, with indicated boundaries. The wall on the deck is simulated as a domain boundary, hence the deck of the model is not included beyond the wall. It is assumed that this simplification does not influence the flow on the deck. Despite the symmetry of the computational domain with respect to the longitudinal plane, the violent flow occurring on deck during the green water phenomenon is not necessarily symmetric. Hence, the full domain is simulated as opposed to only half. The characteristics of fine grids for

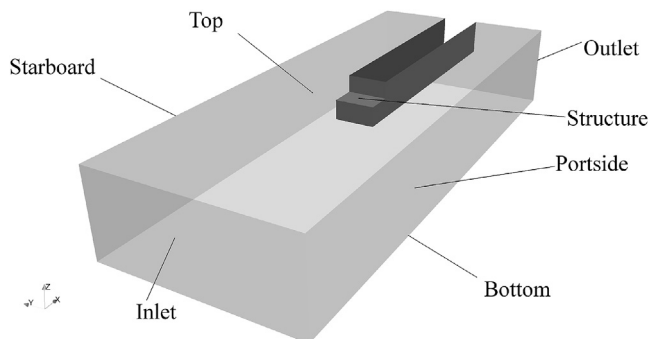


Fig. 2. Computational domain.

Table 2
Computational grid characteristics.

Wave ID	L , m	L_R , m	H , m	$\lambda/\Delta x$	$a/\Delta z$	Δz_{deck} , m
1	6.5	2.5	0.15	375	15.5	$5.84 \cdot 10^{-4}$
2	6.5	2.5	0.15	375	19.4	$5.84 \cdot 10^{-4}$
3	6.5	2.5	0.30	225	23.3	$1.36 \cdot 10^{-3}$
4	7.7	3.1	0.30	333	20.7	$1.34 \cdot 10^{-3}$
5	7.7	3.1	0.60	333	16.3	$3.92 \cdot 10^{-3}$
6	7.7	3.1	0.60	333	19.5	$7.91 \cdot 10^{-3}$
7	14.0	4.0	0.60	354	15.8	$2.24 \cdot 10^{-3}$
8	14.0	4.0	0.60	354	19.8	$2.24 \cdot 10^{-3}$
9	14.0	4.0	0.60	354	27.3	$4.28 \cdot 10^{-3}$

all wave cases are presented in Table 2. Here, L is the domain length, while L_R indicates the length of inlet and outlet relaxation zones. $\lambda/\Delta x$ and $a/\Delta z$ denote the number of cells per wave length and wave amplitude, respectively. H denotes the height of the domain above the deck in metres, where different heights are used depending on the wave amplitude and expected wave run-up against the wall. The freeboard height is 0.045 m above the free surface (Lee et al., 2012). Δz_{deck} denotes the height of the cell above the deck. At certain height from the deck, the cell height is linearly increased towards the top boundary in order to reduce the number of cells. Also, the cell size is reduced linearly in the horizontal direction from the inlet boundary towards the structure. Hence, $\lambda/\Delta x$ is measured next to the structure. Fig. 3 shows the computational grid in the longitudinal central plane and on the surface of the structure used for wave 4. Note that the coarse grid is presented for better visibility of grid lines. The simple geometry of the structure enables fully structured and orthogonal grids to be generated.

Depth and breadth of the domain are constant for all wave cases, where the depth is $D = 1$ m, and breadth $B = 3$ m. It should be noted here that the depth of the wave tank in the experiments was 3.5 m, however only 1 m is included in the simulation in order to save computational time. To avoid influence of this simplification, wave velocity from the stream function wave theory is prescribed at the bottom in order to make it transparent to the flow. This treatment assumes that the diffracted wave field is negligible at the depth of 1 m. Similarly, the breadth is also reduced from 8 to 3 m, with relaxation zones near the starboard and portside boundaries preventing reflection of the diffracted wave field.

Considering the violent free surface flows at the deck, and the explicit nature of the isoAdvector method, the time step is adjusted during the simulation to maintain a maximum fixed Courant–Fredrich–Lewy (CFL) number of $C_o = 0.75$. The same C_o is used in all simulations and on all grids, which results in consistent time step variation on different grids. For reference, average time-step for wave 1 on fine grid is 0.0006 s, while for wave 9 it is 0.001 s.

As indicated in Fig. 1, the circular pressure gauges are 18 mm in diameter. Cells used on the deck are rectangular, where the horizontal

dimensions of the cell, which correspond to the spatial discretisation of the deck surface, ranges from 4 to 13 mm, depending on the grid. Hence, the deck surface discretisation resolution is always higher compared to the area of the pressure gauge used in the experiment. As stated in (Lee et al., 2012) the sampling rate of pressure gauges used in the experiment is 5 kHz, corresponding to a time-step of 0.0002 s, which is comparable to time-steps used in the simulations.

No turbulence modelling is used in this work since it can be considered to have a negligible influence on pressure distribution at the structure. Moreover, the pressure and velocity gradients in the flow on deck are extremely violent, rendering standard single-phase, wall bounded models inapplicable. The influence of turbulence should, however, be investigated in the future.

4.2. Uncertainty analysis

The total numerical uncertainty is dominated by discretisation and periodic uncertainty, since the iterative uncertainty is kept low by using sufficient number of nonlinear correctors per time-step and converging linear systems to a tight tolerance ($\approx 10^{-9}$). In order to assess the discretisation uncertainty, a grid and time-step refinement uncertainty study is performed with the least squares approach developed by Eca & Hoekstra (Eça and Hoekstra, 2014). In case of unsteady flow, the time-step has to be varied as well as the grid resolution (Eça and Hoekstra, 2008). In this work the time-step is reduced simultaneously with the cell size by maintaining a fixed CFL number. For the least squares approach, at least four refinement levels are needed in order to calculate the uncertainty. Constant refinement ratio of $r = \sqrt{2}$ is used for all wave cases, which is defined as the ratio between spatial and temporal resolution between adjacent refinement levels: $r = h_{i-1}/h_i = \tau_{i-1}/\tau_i$, where h_i stands for the representative cell size of refinement level i , while τ_i stands for the time step. Since C_o changes linearly with the cell size, τ also varies linearly, hence the condition $r = \tau_{i-1}/\tau_i$ is satisfied. Table 3 lists the number of cells for all grids and wave cases. All simulations were performed on processors Intel Xeon E5-2637 v3 15M Cache 3.50 GHz. CPU time per wave period on eight cores for the coarse grid ranges between 1.3 and 1.9 h, while on the fine grid it ranges from 7.3 to 15.6 h, depending on the wave case.

According to Eca & Hoekstra (Eça and Hoekstra, 2014), the uncertainty assessment begins with assessing the error of discretisation:

$$\varepsilon_i = \alpha h_i^p, \quad h_i^* = (\tau_i h_i^2)^{1/3}, \tag{11}$$

using the least squares fit. Here, α is an unknown constant, and p is the obtained order of accuracy. The least squares fit is obtained by minimising the following function:

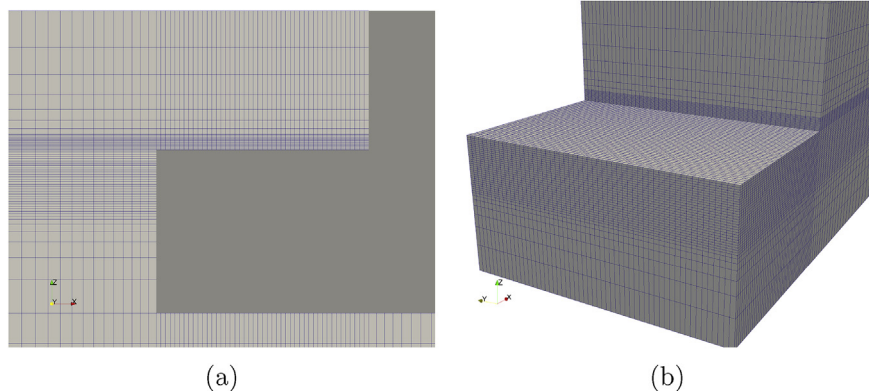


Fig. 3. Computational grid for wave 4 case: a) grid in the longitudinal central plane, b) surface grid of the structure.

Table 3
Grid sizes used in the uncertainty analysis.

Wave ID	Number of cells			
	Grid 1	Grid 2	Grid 3	Grid 4
1	498 720	948 780	1 969 077	3 928 939
2	498 720	948 780	1 969 077	3 928 939
3	276 699	518 476	1 077 515	2 181 103
4	291 546	546 952	1 140 179	2 299 683
5	319 035	603 876	1 236 052	2 509 667
6	238 617	453 796	934 552	1 887 253
7	627 009	1 181 376	2 313 248	4 561 172
8	627 009	1 181 376	2 313 248	4 561 172
9	484 674	905 268	1 754 384	3 454 682

$$S(\phi_0, \alpha, p) = \sqrt{\sum_{i=1}^N (\phi_i - (\phi_0 + \alpha h_{si}^p))^2}, \tag{12}$$

where ϕ_0 denotes the estimate of the exact solution, while N denotes the number of refinement levels. Minimisation of Eq. (12) leads to a nonlinear system of equations, which needs to be solved iteratively. In case the observed order of accuracy p is larger than two, the first or second order terms are used, i.e. the following are solved:

$$\begin{aligned} \varepsilon_{1,i} &= \alpha h_{si}^p, \\ \varepsilon_{2,i} &= \alpha h_{si}^{2p}, \end{aligned} \tag{13}$$

and the fit with smaller standard deviation is used. If $p < 0.5$, first and second order terms are retained in addition to Eq. (13):

$$\varepsilon_{12,i} = \alpha_1 h_{si}^p + \alpha_2 h_{si}^{2p}, \tag{14}$$

where the fit with the smallest standard deviation is used. Standard deviation is calculated as:

$$\sigma = \sqrt{\frac{\sum_{i=1}^N (\phi_i - (\phi_0 + \alpha h_{si}^p))^2}{N - 3}}. \tag{15}$$

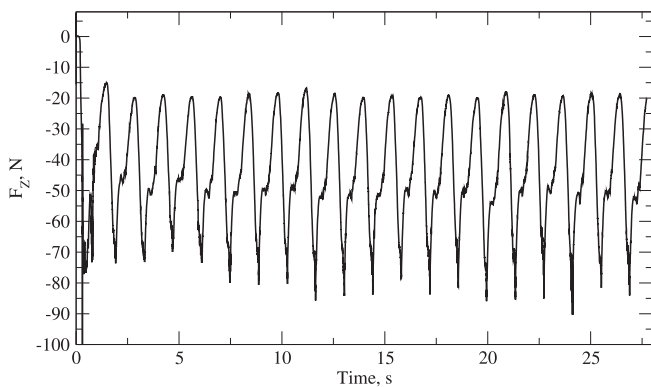


Fig. 4. Vertical force exerted on deck for wave 6.

Table 4
Discretisation uncertainties for vertical force peak and integral measured on the deck.

Wave ID	$F_{0,max}$, N	$U_{CD,F}$, %	I_0 , Ns	$U_{CD,I}$, %
1	21.83	8.8	22.02	0.4
2	37.45	15.0	36.27	11.4
3	62.25	5.3	59.45	8.5
4	39.56	12.7	42.21	20.7
5	61.09	2.2	61.03	4.4
6	163.27	35.8	105.95	16.0
7	72.07	1.4	71.66	0.3
8	159.93	0.2	115.61	0.03
9	284.39	8.2	166.02	1.9

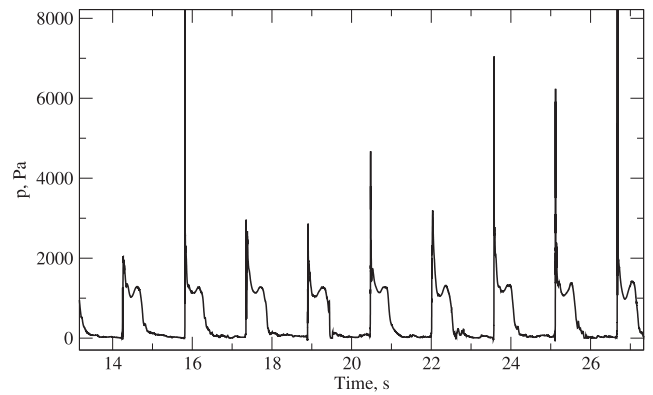


Fig. 5. Pressure signal at gauge 7 for wave 9.

Once ε , ϕ_0 and σ are known, the uncertainty of the result can be established. If the data is well behaved, the following expression is used for assessing the refinement uncertainty:

$$U_i = F_S \varepsilon_i + \sigma + |\phi_i - \phi_{fit}|, \tag{16}$$

where F_S is the safety factor, while ϕ_{fit} presents the least squares fitted value of the solution for grid i . The data is well behaved if $\sigma < \Delta$, where Δ expresses the data range:

$$\Delta = (\phi_{max} - \phi_{min}) / (N - 1), \tag{17}$$

where ϕ_{max} and ϕ_{min} represent the maximum and minimum value from all refinement levels. In case the data is not well behaved, i.e. $\sigma > \Delta$, the uncertainty is assessed as:

$$U_i = 3 \frac{\sigma}{\Delta} (\varepsilon_i + \sigma + |\phi_i - \phi_{fit}|). \tag{18}$$

In this work the uncertainty is assessed for the finest refinement level, i.e. in the above expressions $i = 4$. Since the discretisation uncertainty study theoretically requires a smooth variable in time, the uncertainty is assessed for the vertical force exerted on the deck, i.e. the spatial integral of pressure, instead of the pressure measured at gauge locations.

Total computational uncertainty is assessed as the superposition of the discretisation and periodic uncertainty:

$$U_{CT} = \sqrt{U_{CD}^2 + U_{CP}^2}, \tag{19}$$

where U_{CD} denotes the discretisation uncertainty established using Eq. (16) or Eq. (18), while U_{CP} represents the periodic uncertainty calculated

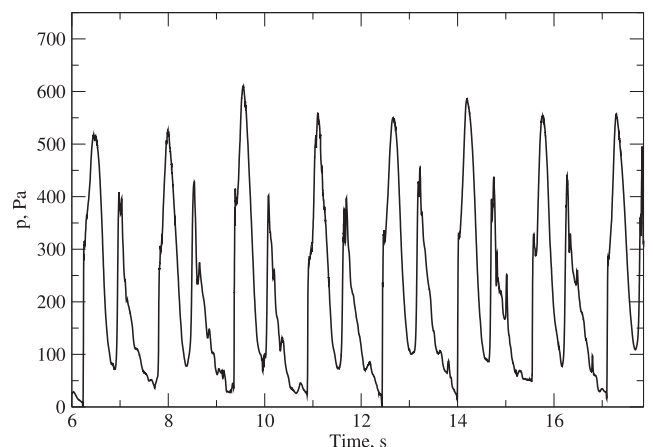


Fig. 6. Pressure signal at gauge 1 for wave 9.

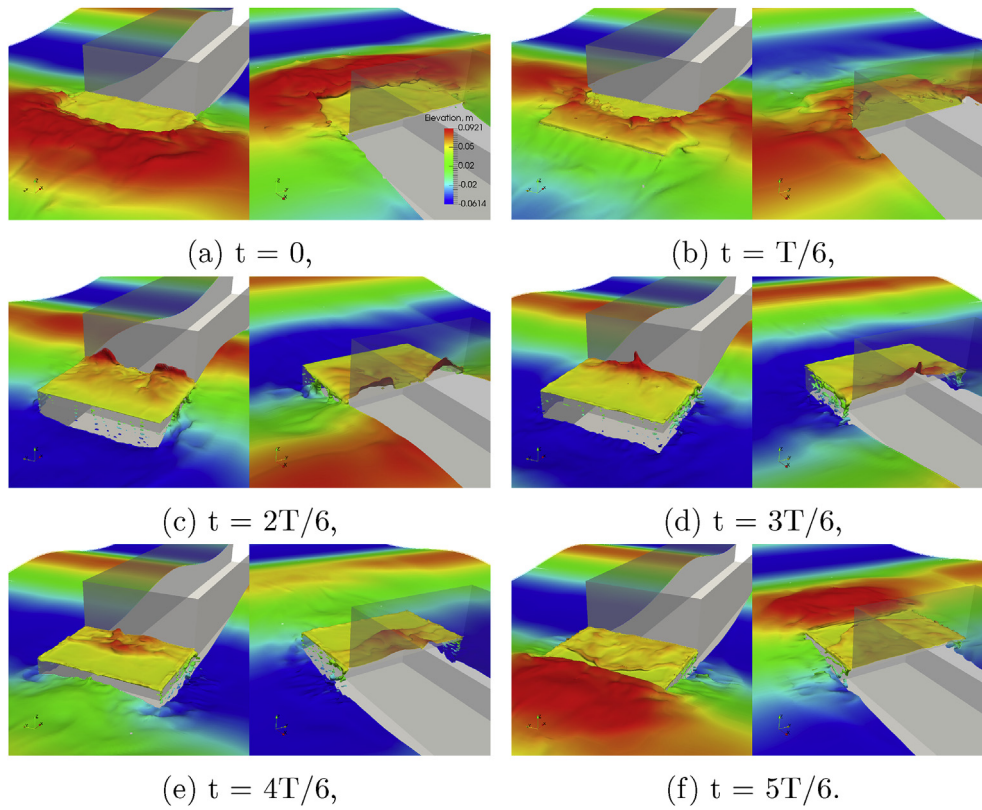


Fig. 7. Perspective view of the green sea event for wave 3.

in the same manner as for the experimental data:

$$U_{CP} = \frac{\phi_{\max} - \phi_{\min}}{N_C}, \quad (20)$$

where N_C denotes the number of periods included in the analysis. Fig. 4 shows the signal of vertical force acting on the deck for wave 6. For every wave case, 20 wave periods are simulated, where the last 14 are used in the analysis to avoid initial transient effects.

Numerical discretisation uncertainties calculated with the vertical force on deck are summarised in Table 4 for all wave cases, where $F_{0,\max}$ denotes the estimated exact solution (corresponding to ϕ_0 in Eq. (12)) of vertical force peak F_{\max} , while I_0 denotes the estimated exact solution for the force integral, i.e. force impulse. F_{\max} and I are calculated as:

$$F_{\max} = \frac{\sum_{i=1}^{N_C} F_{i,\max}}{N_C}, \quad (21)$$

$$I = \frac{\sum_{i=1}^{N_C} \int_0^T F_i(t) dt}{N_C}, \quad (22)$$

where $F_{i,\max}$ denotes the force peak for period i , while T denotes the wave period. In Table 4, $U_{CD,F}$ and $U_{CD,I}$ denote the discretisation uncertainty for force peak F_{\max} and force impulse I , respectively. Uncertainties show large differences from one wave case to another, however they remain below 10% for most items, and go as low as 0.03%. The outliers are wave 4 and 6 with uncertainties higher than 10%.

4.3. Results

As stated earlier, two sets of results are compared within this study:

- The average pressure peak during one period:

$$p_{\max} = \frac{\sum_{i=1}^{N_C} P_{i,\max}}{N_C}, \quad (23)$$

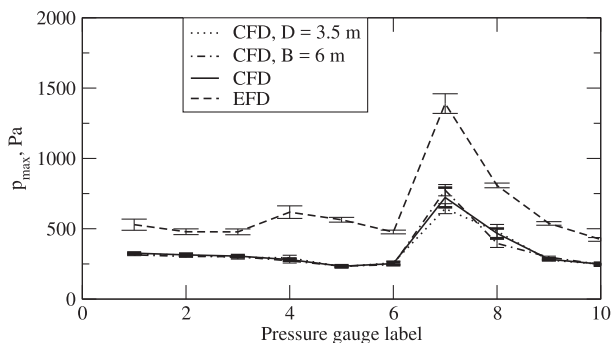


Fig. 8. Pressure peak comparison between different domain sizes for wave 7.

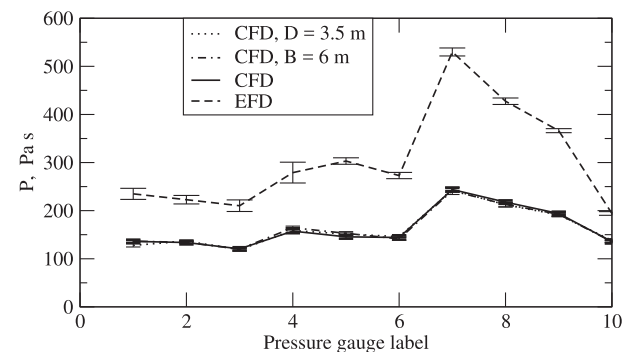


Fig. 9. Pressure integral comparison between different domain sizes for wave 7.

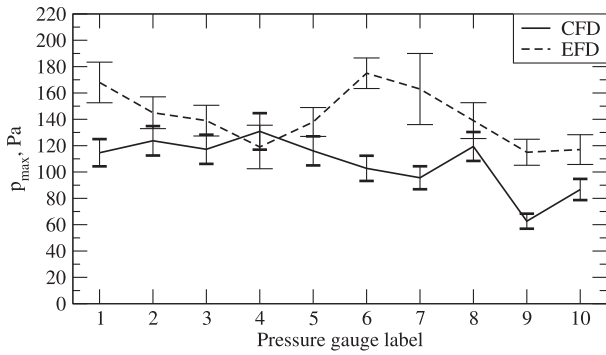


Fig. 10. Pressure peak results comparison for wave 1.

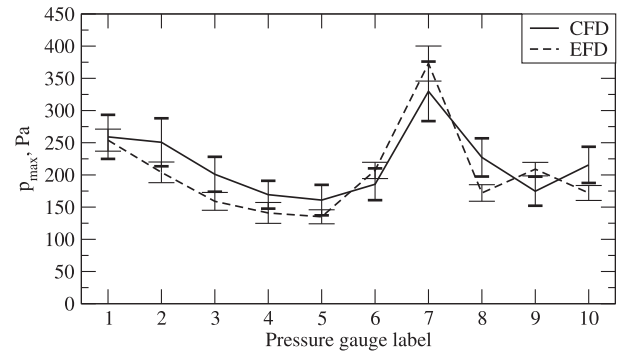


Fig. 13. Pressure peak results comparison for wave 4.

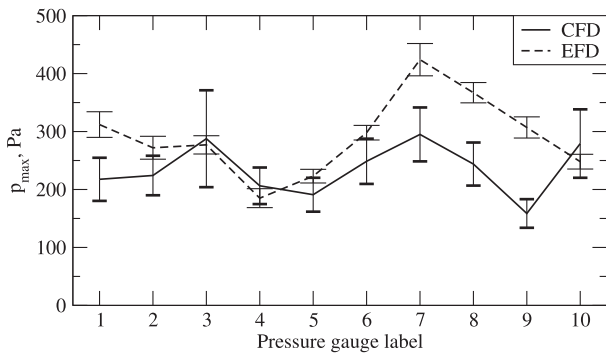


Fig. 11. Pressure peak results comparison for wave 2.

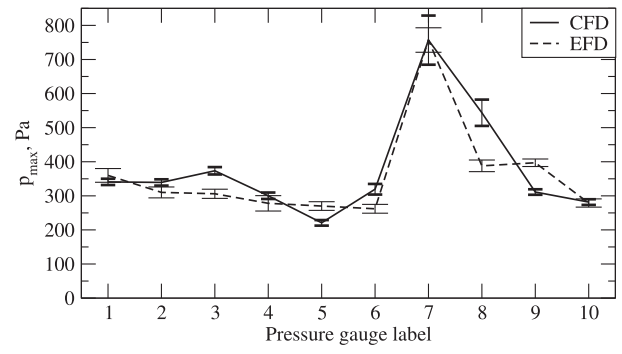


Fig. 14. Pressure peak results comparison for wave 5.

where $p_{i,max}$ denotes the pressure peak during i -th wave period.

- The average pressure time integral over one wave period:

$$P = \frac{\sum_{i=1}^{N_c} \int_0^T p_i(t) dt}{N_c} \quad (24)$$

Although the pressure peak that occurs during green sea event is an obvious quantity for comparison, it is not necessarily relevant for the structural response. If the pressure peak lasts a very short amount of time, it will not influence the structural response. On the other hand, it is a known fact that in numerical simulations, high pressure peaks can occur when a free surface impacts against a solid boundary. Hence, to provide a more complete comparison, the pressure integral in time is also compared. Fig. 5 shows an example of the pressure signal in time measured by gauge 7 for wave 9, where extremely transient pressure peaks can be seen. Large differences in pressure peaks increase the periodic pressure peak uncertainty, which is observed in the results shown below. However, the integral of pressure in time is not sensitive to high

transient peaks. For gauges further away from the wall, pressure peaks are less prominent, as shown in Fig. 6 where gauge 1 pressure signal is shown for the same wave case.

In order to accurately capture the total pressure at the horizontal deck during a complete wave period, it is necessary to capture the thinnest layer of water that can occur during the wave recession from the deck. In order to achieve that, at least one cell centre is needed between the free surface and deck at all times. It can be observed in Table 2 that different cell sizes are used at the deck for different wave cases. The minimum depth of water on deck depends on wave amplitude and period. Waves with shorter period give a smaller amount of time for the water to pour down from the deck. Similarly, larger wave amplitude implies more water on deck. Fig. 7 sequentially shows one period of a green sea event for wave 3, where the thin layer of water can be seen after the collapse of water run-up against the wall.

4.3.1. Influence of the domain size

As stated earlier, breadth and depth of the domain were reduced with respect to experimental setup in order to reduce the number of cells. The

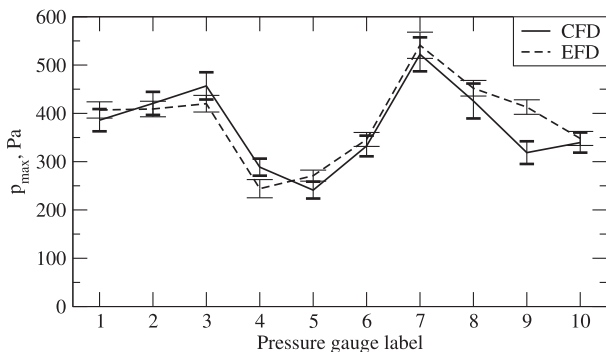


Fig. 12. Pressure peak results comparison for wave 3.

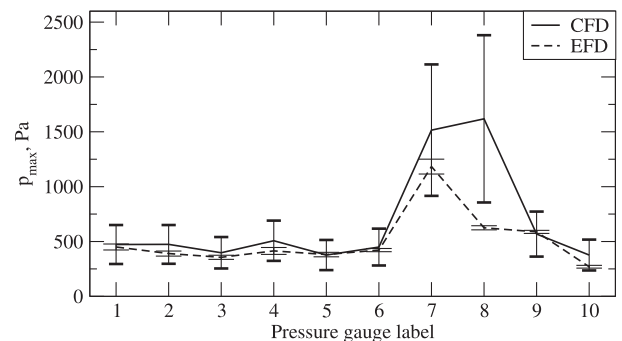


Fig. 15. Pressure peak results comparison for wave 6.

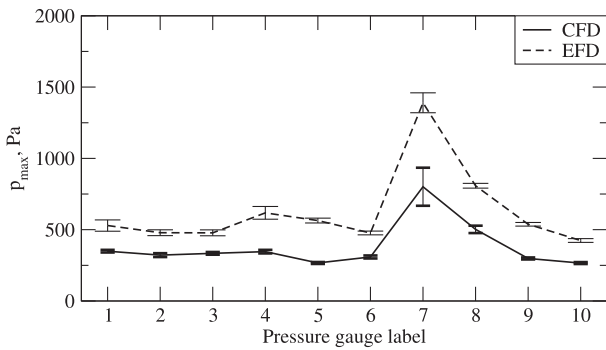


Fig. 16. Pressure peak results comparison for wave 7.

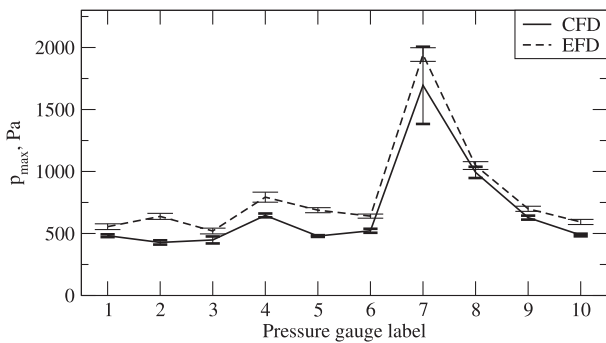


Fig. 17. Pressure peak results comparison for wave 8.

breadth was reduced from 8 to 3 m, while the depth of 1 m is used instead of 3.5 m. Depth was reduced by prescribing the incident wave velocity at the bottom boundary, hence the wave diffraction effects were neglected from this depth on. Breadth was reduced where similar boundary condition is imposed: relaxation zones were prescribed near the side boundaries in order to eliminate diffracted waves and prevent reflection.

In order to test the validity of these assumptions, and to assess their influence on pressure results, two additional tests are performed with different domain breadth and depth. Tests are performed for one wave only on the coarsest refinement level. Wave 7 case is used for this comparison for two reasons: it is in the group of longest waves, where limited depth could have the greatest influence, and because it exhibited poorest agreement with the experiment, as shown below. Hence, if these assumptions are not valid, an improvement in result quality should be exhibited.

The first test is performed by increasing the breadth of the computational domain from 3 to 6 m, while keeping the rest of the dimensions fixed. Side boundary conditions and size of the relaxation zones are not changed. In the second test the depth is increased from 1 m to 3.5 m, corresponding to the experimental setup. In this case the velocity

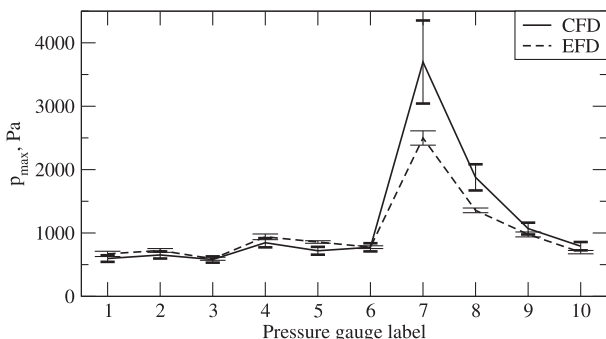


Fig. 18. Pressure peak results comparison for wave 9.

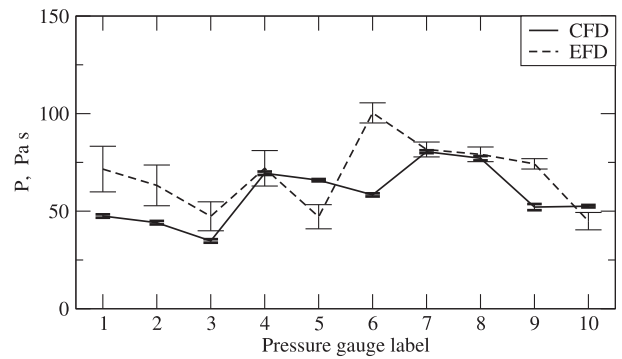


Fig. 19. Temporal pressure integral results comparison for wave 1.

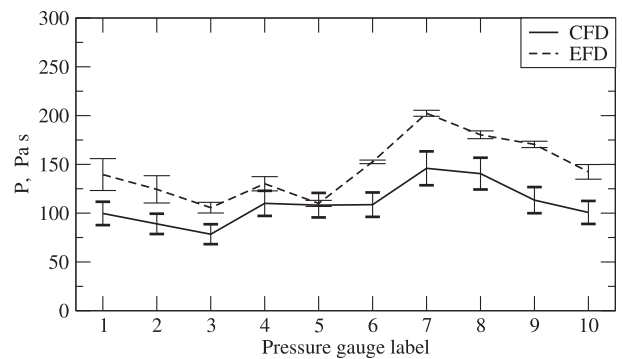


Fig. 20. Temporal pressure integral results comparison for wave 2.

boundary condition on the bottom is changed from incident wave velocity to non-slip, non-permeable wall boundary condition.

Fig. 8 shows the comparison of the three CFD results and experimental results for pressure peaks. Results denoted with CFD correspond to the original setup used in this study, obtained on the coarsest refinement level. The remaining two CFD results are denoted with the changed dimension with respect to the original setup. The influence of the domain size is almost none for most wave gauges, except for gauge 7 and 8 where a very small change is observed.

Fig. 9 shows the comparison for pressure integrals. The variation of the domain size had a negligible influence on the pressure integrals for all gauges. Hence, the simplifications made to reduce the number of cells had no influence on the results, and are justified.

4.3.2. Pressure peaks

The comparison of pressure peak results with corresponding uncertainties are shown in Figs. 10–18. Complete results with uncertainties are given in tabular form in Sec. A.1. The average value of the pressure

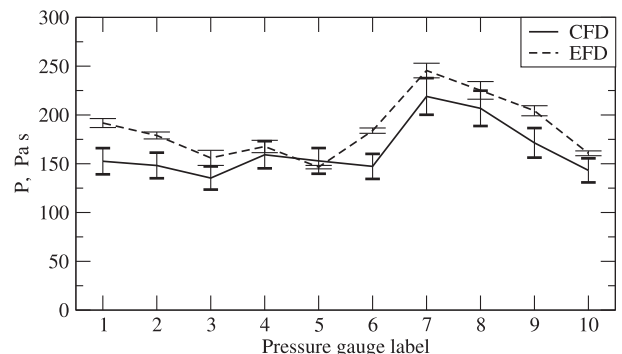


Fig. 21. Temporal pressure integral results comparison for wave 3.

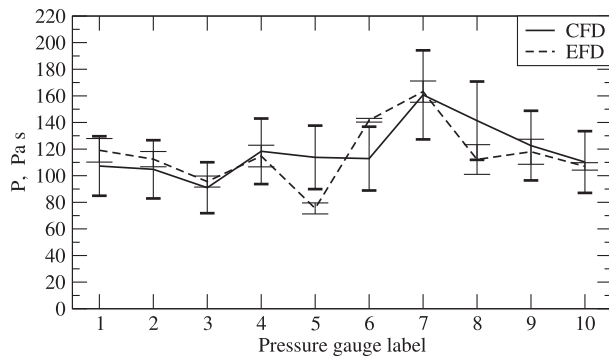


Fig. 22. Temporal pressure integral results comparison for wave 4.

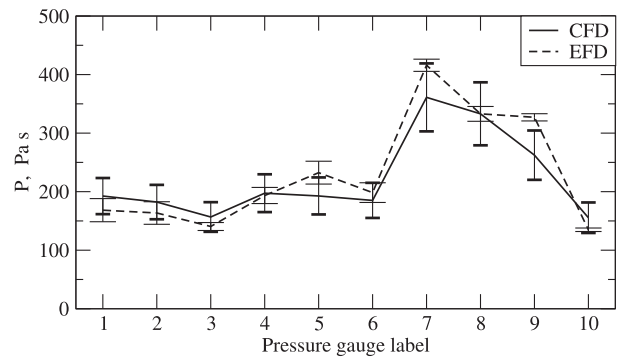


Fig. 24. Temporal pressure integral results comparison for wave 6.

peak is denoted on the y-axis while the x-axis denotes the index of the pressure gauge as indicated in Fig. 1. The error bars present the total numerical and experimental uncertainties, Eq. (19) and Eq. (10), respectively. CFD stands for the result obtained using the present numerical methods, while EFD stands for Experimental Fluid Dynamics.

Results for wave 1 are presented in Fig. 10. Relative differences between the results are considerable, however the absolute difference is not large since the pressure load for this case is small. The uncertainties are similar for most gauges, except for a few where experimental results exhibit higher uncertainties. This wave case has the smallest amplitude, requiring higher mesh resolution. Pressure peaks for wave 2 shown in Fig. 11 show similar agreement as wave 1, with slightly larger numerical uncertainties.

For wave 3, results in Fig. 12 show good agreement with experimental results. For eight out of nine gauges the uncertainty intervals overlap, and the trend is very well captured.

Wave 4 shows good agreement in Fig. 13, where uncertainty intervals overlap for all gauges, while the uncertainties are similar between the numerical and experimental result.

For wave 5, pressure peaks in Fig. 14 correspond well to experimental data, with gauge 8 and 9 showing larger discrepancies. Gauge 7, 8 and 9 are located close to the wall, where the most violent flow occurs, making the pressure in that area more challenging to predict and increasing the periodic uncertainties.

For wave 6, both experimental and numerical results shown in Fig. 15 predict considerably higher pressure peaks for gauge 7 near the wall than the gauges further from the wall. Results agree well for gauges further from the wall, however significant over-estimation is observed for gauges 7 and 8, as well as high uncertainties. The high uncertainties for gauges 7 and 8 are the consequence of extremely transient pressure peaks in the numerical result as shown in Fig. 5. For this case, numerical uncertainties are relatively large for all gauges due to high grid uncertainties, as shown in Table A6.

Unlike other cases, results for wave 7 show significant underestimation when comparing to the experimental data, as shown in Fig. 16. The

trends, however, are well captured. The uncertainties are generally smaller than experimental uncertainties, except for gauges 7 and 8.

For wave 8 the results shown in Fig. 17 show good agreement with the experiment with low uncertainties, where gauge 7 stands out with higher uncertainties. In this case, as for wave 7, the pressure peaks are underestimated, but the difference is significantly smaller. As in majority of cases, the trend is well captured.

Wave 9 exhibits good agreement for gauges further from the wall as shown on Fig. 18, whereas gauges next to the wall show over-prediction with larger uncertainties originating mostly from periodic uncertainties (see Table A9). The over-prediction might also be related to compressibility effects, which will be investigated in the future.

4.3.3. Pressure integrals

The comparison of integrals of pressure in time for all wave cases is shown in Figs. 19–27. Complete results with uncertainties are given in tabular form in Sec. A.2. Same as for the pressure peaks, the x-axis on the graphs denotes the pressure gauge label, while integral of pressure P is shown on the y-axis.

The numerical results of pressure integrals for wave 1 shown in Fig. 19 exhibit very low uncertainties, while the agreement with experimental results is similar as for pressure peaks.

For wave 2, results in Fig. 20 show that the trend is well captured, while the values are somewhat underestimated. Numerical uncertainties are similar for all gauges.

In Fig. 21, pressure integrals for wave 3 show good agreement with the experiment, with smaller uncertainties for experimental measurements. For this wave case, pressure peaks show better agreement than the time integrals, which are generally underestimated.

For wave 4, good agreement is achieved as indicated in Fig. 22, with higher numerical uncertainties comparing to the experiment. The high numerical uncertainties originate from discretisation uncertainties, while periodic uncertainty has a minor contribution (see Table A13).

For wave 5, Fig. 23 shows good agreement with overlapping

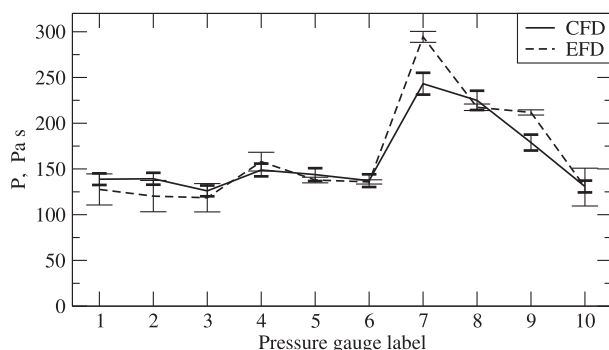


Fig. 23. Temporal pressure integral results comparison for wave 5.

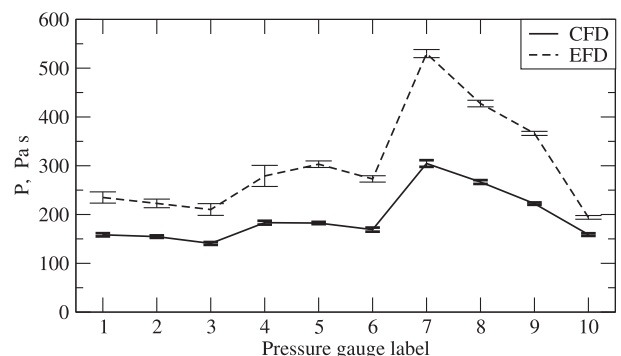


Fig. 25. Temporal pressure integral results comparison for wave 7.

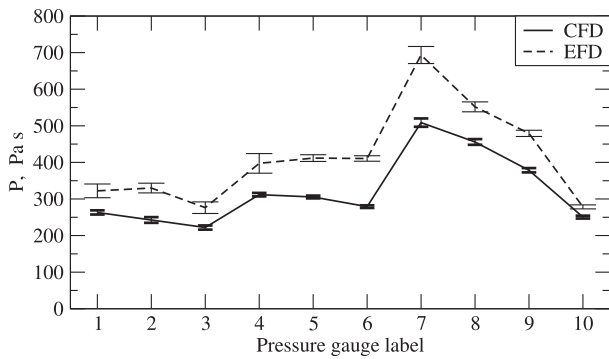


Fig. 26. Temporal pressure integral results comparison for wave 8.

uncertainty intervals, except for gauge 7 and 9. Numerical uncertainties are generally smaller than experimental for this case.

In Fig. 24 uncertainty intervals for wave 6 are overlapping for nine out of ten gauges, the only outlier being gauge 9. Same as for pressure peaks for this wave case, numerical uncertainties are larger than experimental due to large grid uncertainty.

As for pressure peaks, wave 7 exhibits considerable under-estimation for pressure integrals shown in Fig. 25, with small uncertainties and good prediction of the trend. The consistent underestimation of pressure in this case should be investigated from both numerical and experimental side. The difference might be caused by transversal reflection occurring in the experiment due to finite tank breadth, which is not present in the numerical simulation. Also, compressibility effects may influence the results, hence the effect of compressibility will be investigated in the future.

Wave 8 again shows good trend agreement and low uncertainties in Fig. 26, however the values are underestimated. Larger difference is observed in this case than for pressure peaks.

For wave 9 shown in Fig. 27 the trend is well captured with lower numerical uncertainties than experimental results. Unlike pressure peaks, here the values are underestimated for most gauges, except gauge number 10.

4.4. Discussion

Overall the results for both pressure peaks and integrals exhibit good agreement with the experimental data. Pressure peaks compare better with experiments for pressure gauges further from the wall, where the influence of water impingement is smaller. However, for waves 1 to 5 the peaks are well predicted even close to the wall with acceptable uncertainties, while waves 6 to 9 exhibit higher uncertainties and deviations for pressure gauge 7, which is next to the wall and at the centre line. Wave 6 shows very large deviation and uncertainty for gauge 8, which is an outlier in the results, and should be investigated. For long waves, i.e. 7 to 9, pressure peaks exhibit small uncertainties and well

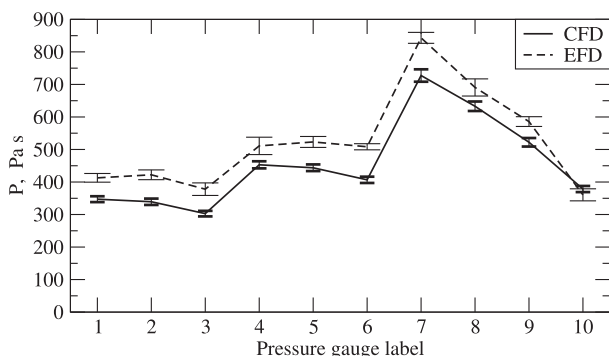


Fig. 27. Temporal pressure integral results comparison for wave 9.

Table 5 Overall result comparison.

Wave ID	E_{pmax} , Pa	E_{pmax} , %	E_p , Pas	E_p , %
1	37.21	25.61	15.20	22.65
2	68.75	21.91	36.33	24.13
3	30.56	8.46	23.73	12.61
4	34.58	18.64	13.44	13.04
5	48.90	14.76	14.65	7.89
6	172.52	29.82	25.63	11.14
7	251.12	39.10	109.96	34.59
8	130.79	17.31	93.31	21.88
9	229.60	15.84	71.80	13.99

captured trends. The results agree well with the experimental data for wave 8 and 9, while wave 7 shows significant under-estimation.

Pressure integrals are predicted well for all gauges for waves 1 to 6, where the uncertainty intervals overlap. Trends agree with experiments as well, except for waves 1 and 4, where difference in trends is observed. For waves 7 to 9 the uncertainties are very low and the trends are captured accurately, however the values are significantly underestimated. The under-estimation is smaller for higher amplitudes, i.e. wave 7 shows the largest difference. This consistent underestimation of pressure for waves with $\lambda = 3.75$ m will be investigated in the future. The difference could indicate an inconsistency between the numerical simulations and experiments with regards to the wave elevation and reflection.

Regarding wave steepness in individual cases, no correlation can be seen in the graphs between trends of the curves, discrepancies and wave steepness. On the other hand, the trends show similarities between waves with the same wave length, while the wave height only influences the magnitude of pressure loads. Thus, it can be concluded that wave celerity has a larger influence on the character of the green water event than wave steepness in this case.

Overall summary of pressure peak and integral result comparison is given in Table 5. For each wave the average absolute and relative difference between numerical and experimental result across all pressure gauges is given. E denotes the difference of numerical and experimental result which is expressed in absolute values and in percentages relative to the experimental result, where the indices $pmax$ and P stand for pressure peak and integral, respectively. For pressure peaks, absolute difference ranges from 30 to 70 Pa for wave cases 1 to 5, while the difference increases for waves 6 to 9, ranging from 130 to 250 Pa. However the relative differences show smaller variation, except for wave 7 where larger discrepancies occur. Average relative difference for pressure peaks for all cases is 21%. Pressure integrals show smaller relative differences with the average difference across all wave cases of 18%. From the practical engineering point of view, the differences for small waves, 1, 2 and 3 are of smaller importance due to the small absolute value of pressure loads. On the other hand, larger differences for waves 6 and 7 should be investigated further since these would have a larger influence on the structural design due to higher absolute pressure loads.

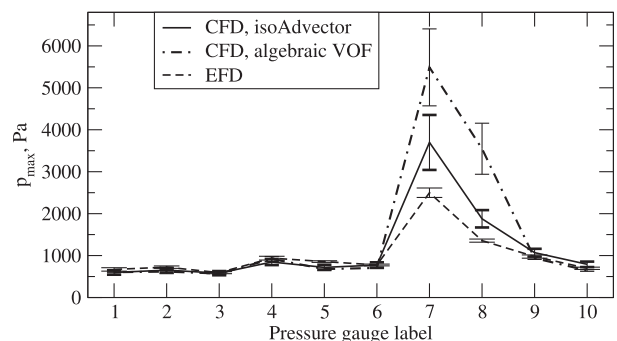


Fig. 28. Pressure peak comparison between the isoAdvector and the algebraic VOF method for wave 9.

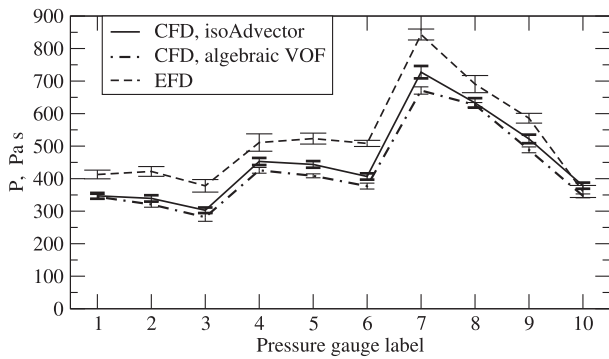


Fig. 29. Pressure integral comparison between the isoAdvector and the algebraic VOF method for wave 9.

4.5. Influence of the interface advection method

To compare the performance of the isoAdvector method for interface advection, an additional simulation is carried out for wave 9, where conventional algebraic VOF method is used with interface compression (Rusche, 2002). Fig. 28 shows the pressure peak results for wave 9 where in addition to experimental and numerical results, the numerical results with conventional algebraic VOF are given. Fig. 29 presents the comparison of the temporal integral of pressure. Note that in these graphs only the periodic uncertainty is included for numerical results, since the

refinement study has not been performed with the algebraic VOF method. The results are similar for pressure peaks except for pressure gauges 7 and 8, where higher values are obtained with the algebraic VOF. Pressure integral results agree well between the two simulations, however the algebraic VOF exhibits slightly larger underestimation with respect to the experimental data. Fig. 30 sequentially shows a visual comparison of volume fraction field α for simulation where isoAdvector and algebraic VOF are used. With isoAdvector, the interface is confined within a single cell even when very violent free surface flow occurs. With algebraic VOF, the interface is smeared, and the geometry of the free surface is described less precisely.

Being a more complex method, isoAdvector requires a larger number of operations comparing to the algebraic VOF. Hence, an increase in CPU time is expected. Both simulations are performed using 24 cores on Intel Xeon Processor E5-2637 v3. Simulation with the algebraic VOF took 37.5 h, while the simulation using isoAdvector took 45 h to compute. Hence, an increased cost of 20% is exhibited in this case. Note that the increase in computational cost depends on the cost of the pressure-velocity coupling algorithm used in the solution procedure.

5. Conclusion

A comprehensive set of numerical simulations of green sea loads have been conducted using the FV based CFD software called Naval Hydro pack which is based on foam-extend. The Ghost Fluid Method is applied for discretisation of the free surface boundary conditions, while the geometric isoAdvector method is used for interface capturing.

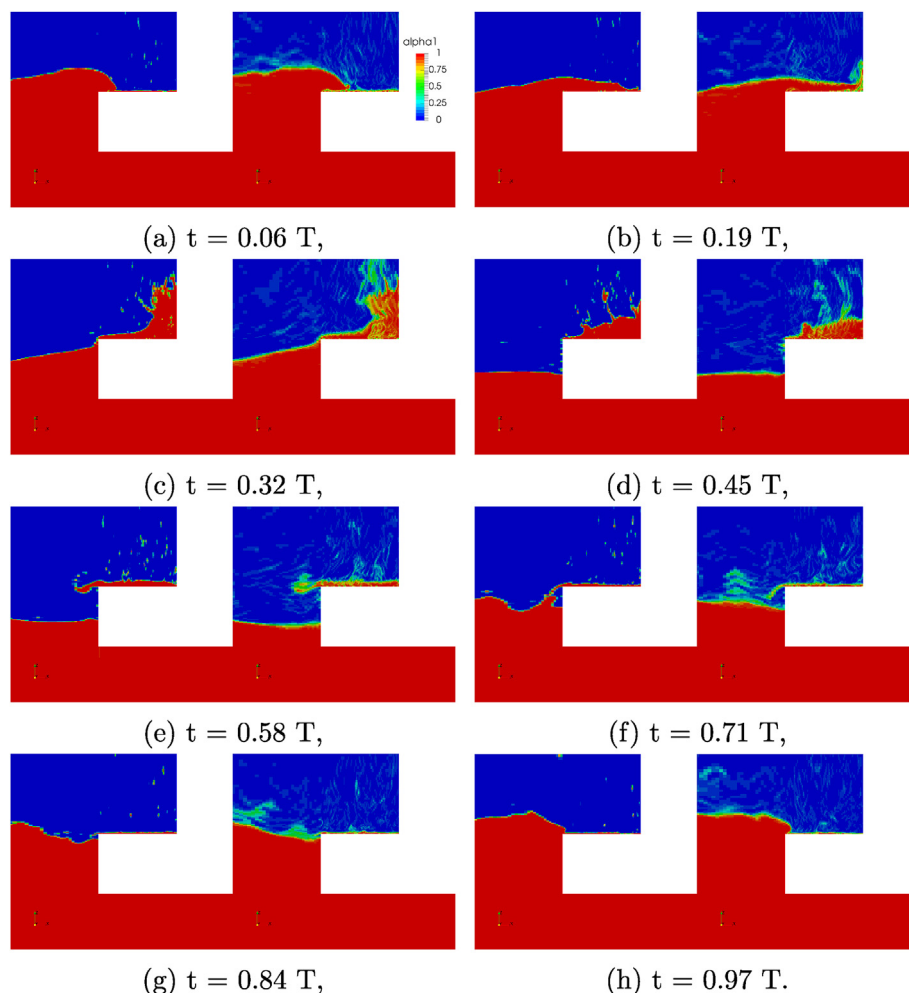


Fig. 30. Visual comparison of the volume fraction field α (denoted "alpha") in simulation where the isoAdvector (left) and the algebraic VOF method (right) are used.

All results are compared to experimental data in order to validate the present method for green sea load calculation. A case of a static, simplified FPSO model is used with a breakwater on deck, with regular incident waves. Nine wave cases are analysed with varying amplitude and steepness, where the pressure at ten locations on deck is measured. Uncertainties are assessed for both experimental and numerical data, yielding a comprehensive comparison. Detailed uncertainty analysis of numerical results is performed via grid and time-step resolution study, as well as periodic uncertainty analysis.

Compared pressure-related quantities are the average pressure peak and time integral of pressure during the wave period. Comparison of pressure peaks shows good overall agreement with comparable uncertainties between experimental and numerical data. Trends of peak pressure across pressure gauges agree well with experiments for seven out of nine wave cases, where the two smallest waves, wave 1 and 2 showed some discrepancy. Values and uncertainty intervals overlap for the majority of pressure gauges for waves 3, 4, 5, 6 and 9. Waves 1 and 2 show reasonable agreement, while waves 7 and 8 show underestimation

of experimental results.

For temporal pressure integrals, trends are well captured for waves 2, 3, 5, 6, 7, 8 and 9, while waves 1 and 4 show slightly different trends. Values correspond well for waves 1, 3, 4, 5 and 6, while integrals for wave 2 and 9 are slightly underestimated. Waves 7 and 8 show larger underestimation which requires further investigation on both numerical and experimental side.

Overall, results show reasonable accuracy and high level of confidence. Comparable uncertainty between numerical and experimental results show that similar precision can be expected in terms of pressure on deck. Future work will involve prediction of realistic green sea loads for offshore objects in irregular waves.

Acknowledgement

The numerical research performed for this work was sponsored by Bureau Veritas under the administration of Dr. Šime Malenica and Dr. Quentin Derbanne.

Appendix. Results in tabular format

Complete results of both numerical and experimental studies are given in this section in tabular form, with break-down of numerical uncertainties.

A.1. Pressure peak results

Table A1
Pressure peak results for wave 1.

Gauge ID	$p_{max,C}$, Pa	U_{CT} , Pa	U_{CD} , Pa	U_{CP} , Pa	$p_{max,E}$, Pa	U_{ET} , Pa
1	114.63	10.35	10.10	2.25	168.00	15.41
2	123.69	11.15	10.90	2.33	145.00	12.06
3	117.26	11.08	10.33	4.00	139.00	11.67
4	130.84	13.85	11.53	7.68	119.00	16.49
5	116.03	11.01	10.23	4.09	138.00	10.97
6	102.78	9.60	9.06	3.17	175.00	11.60
7	95.63	8.70	8.43	2.18	163.00	26.99
8	119.38	10.96	10.52	3.06	139.00	13.61
9	62.66	5.71	5.52	1.47	115.00	9.87
10	86.69	8.04	7.64	2.51	117.00	11.30

Table A2
Pressure peak results for wave 2.

Gauge ID	$p_{max,C}$, Pa	U_{CT} , Pa	U_{CD} , Pa	U_{CP} , Pa	$p_{max,E}$, Pa	U_{ET} , Pa
1	217.51	37.26	32.55	18.15	312.00	22.15
2	224.13	34.16	33.54	6.48	272.00	19.81
3	287.62	83.59	43.04	71.66	277.00	15.76
4	206.41	31.54	30.89	6.39	185.00	16.31
5	190.97	29.22	28.58	6.09	223.00	11.74
6	248.64	39.06	37.20	11.89	298.00	12.60
7	295.03	46.53	44.15	14.69	424.00	27.91
8	243.91	37.13	36.50	6.85	367.00	17.55
9	158.58	24.65	23.73	6.69	307.00	18.26
10	279.21	59.03	41.78	41.70	248.00	12.75

Table A3
Pressure peak results for wave 3.

Gauge ID	$p_{max,C}$, Pa	U_{CT} , Pa	U_{CD} , Pa	U_{CP} , Pa	$p_{max,E}$, Pa	U_{ET} , Pa
1	385.93	23.06	20.30	10.94	407.00	16.81
2	420.63	23.84	22.12	8.88	409.00	16.12
3	456.87	28.15	24.03	14.66	420.00	17.15
4	288.67	17.66	15.18	9.02	244.00	18.89
5	241.12	17.49	12.68	12.04	271.00	11.44
6	332.49	21.39	17.49	12.32	346.00	14.50
7	522.20	35.21	27.46	22.04	541.00	27.18
8	425.62	36.13	22.38	28.36	452.00	16.12
9	318.71	23.54	16.76	16.53	413.00	15.04
10	339.52	20.77	17.86	10.61	348.00	14.53

Table A4
Pressure peak results for wave 4.

Gauge ID	$p_{max,C}$, Pa	U_{CT} , Pa	U_{CD} , Pa	U_{CP} , Pa	$p_{max,E}$, Pa	U_{ET} , Pa
1	259.10	34.24	32.78	9.89	254.00	17.11
2	250.67	37.25	31.71	19.54	204.00	16.01
3	201.02	27.07	25.43	9.26	159.00	13.87
4	169.31	21.62	21.42	2.95	141.00	16.17
5	160.91	23.66	20.36	12.05	135.00	10.90
6	185.47	24.70	23.46	7.72	207.00	12.64
7	329.82	46.27	41.73	19.99	373.00	27.21
8	227.19	29.67	28.74	7.36	172.00	12.84
9	174.71	22.55	22.10	4.47	209.00	10.54
10	215.57	28.11	27.27	6.80	172.00	11.61

Table A5
Pressure peak results for wave 5.

Gauge ID	$p_{max,C}$, Pa	U_{CT} , Pa	U_{CD} , Pa	U_{CP} , Pa	$p_{max,E}$, Pa	U_{ET} , Pa
1	340.91	9.28	7.63	5.29	360.00	20.15
2	339.31	9.19	7.59	5.18	310.00	16.01
3	373.49	10.82	8.36	6.88	306.00	13.42
4	300.17	9.41	6.72	6.59	278.00	22.48
5	220.82	8.12	4.94	6.44	270.00	12.78
6	319.33	15.67	7.14	13.95	262.00	12.99
7	756.78	72.07	16.93	70.06	757.00	35.95
8	543.68	38.66	12.16	36.70	388.00	17.11
9	311.14	8.13	6.96	4.21	397.00	11.08
10	281.68	8.27	6.30	5.36	279.00	12.08

Table A6
Pressure peak results for wave 6.

Gauge ID	$p_{max,C}$, Pa	U_{CT} , Pa	U_{CD} , Pa	U_{CP} , Pa	$p_{max,E}$, Pa	U_{ET} , Pa
1	472.46	177.72	169.35	53.92	450.00	27.14
2	473.75	176.85	169.81	49.39	390.00	23.25
3	397.45	143.55	142.46	17.66	356.00	18.60
4	507.24	183.41	181.81	24.12	414.00	31.39
5	376.76	137.54	135.05	26.06	381.00	20.42
6	449.28	167.66	161.04	46.65	422.00	14.67
7	1515.21	599.12	543.11	252.93	1183.00	67.99
8	1618.54	762.50	580.15	494.81	625.00	18.74
9	567.73	205.30	203.49	27.17	588.00	13.91
10	376.77	140.75	135.05	39.65	270.00	12.38

Table A7
Pressure peak results for wave 7.

Gauge ID	$p_{max,C}$, Pa	U_{CT} , Pa	U_{CD} , Pa	U_{CP} , Pa	$p_{max,E}$, Pa	U_{ET} , Pa
1	349.21	9.15	5.04	7.63	529.00	39.67
2	321.73	13.29	4.64	12.45	479.00	20.43
3	333.95	9.44	4.82	8.11	478.00	20.77
4	345.99	12.41	4.99	11.36	618.00	44.59
5	266.71	6.72	3.85	5.50	564.00	16.99
6	308.68	10.57	4.46	9.59	477.00	13.32
7	801.19	133.25	11.56	132.75	1390.00	69.72
8	502.13	25.91	7.25	24.87	808.00	16.73
9	298.24	6.79	4.30	5.26	538.00	12.65
10	265.99	6.59	3.84	5.36	424.00	13.20

Table A8
Pressure peak results for wave 8.

Gauge ID	$p_{max,C}$, Pa	U_{CT} , Pa	U_{CD} , Pa	U_{CP} , Pa	$p_{max,E}$, Pa	U_{ET} , Pa
1	482.15	11.23	1.11	11.17	555.00	23.30
2	427.90	17.32	0.99	17.29	638.00	24.35
3	448.10	28.21	1.03	28.19	520.00	23.09
4	645.67	15.46	1.49	15.39	793.00	40.47
5	479.41	6.84	1.11	6.75	688.00	20.56
6	522.08	16.02	1.20	15.98	640.00	16.65
7	1695.05	311.41	3.91	311.39	1943.00	55.10
8	992.93	45.14	2.29	45.08	1048.00	31.46
9	628.03	15.94	1.45	15.87	699.00	20.66
10	487.77	10.80	1.12	10.74	593.00	20.83

Table A9
Pressure peak results for wave 9.

Gauge ID	$P_{max,C}$, Pa	U_{CT} , Pa	U_{CD} , Pa	U_{CP} , Pa	$P_{max,E}$, Pa	U_{ET} , Pa
1	596.71	51.93	48.76	17.88	670.00	41.02
2	652.95	55.40	53.36	14.91	724.00	29.57
3	580.83	49.43	47.46	13.80	593.00	24.23
4	846.06	72.93	69.13	23.21	939.00	44.75
5	719.55	61.81	58.80	19.06	857.00	20.05
6	774.05	64.49	63.25	12.59	776.00	21.67
7	3697.68	655.71	302.15	581.94	2498.00	112.74
8	1877.29	206.91	153.40	138.86	1357.00	36.96
9	1069.49	92.66	87.39	30.79	977.00	38.47
10	791.68	65.44	64.69	9.84	697.00	26.35

A.2. Pressure integral results

Table A10
Pressure integral results for wave 1.

Gauge ID	P_C , Pa s	U_{CT} , Pa s	U_{CD} , Pa s	U_{CP} , Pa s	P_E , Pa s	U_{ET} , Pa s
1	47.52	0.85	0.17	0.84	71.57	11.68
2	44.09	0.89	0.16	0.88	63.22	10.42
3	34.75	0.91	0.13	0.90	47.37	7.43
4	69.44	0.87	0.25	0.84	71.96	9.10
5	65.86	0.59	0.24	0.54	47.15	6.18
6	58.34	0.80	0.21	0.77	100.35	5.16
7	80.47	0.72	0.29	0.66	81.61	3.83
8	77.13	1.12	0.28	1.08	79.12	3.75
9	52.09	1.59	0.19	1.58	74.26	2.65
10	52.57	0.64	0.19	0.61	44.88	4.45

Table A11
Pressure integral results for wave 2.

Gauge ID	P_C , Pa s	U_{CT} , Pa s	U_{CD} , Pa s	U_{CP} , Pa s	P_E , Pa s	U_{ET} , Pa s
1	99.74	11.96	11.39	3.62	139.56	16.38
2	89.01	10.40	10.17	2.16	124.41	13.97
3	78.44	10.25	8.96	4.97	105.65	5.44
4	110.06	12.87	12.57	2.77	130.15	7.31
5	108.17	12.59	12.36	2.43	110.00	3.08
6	108.69	12.49	12.42	1.37	152.58	1.83
7	145.92	17.36	16.67	4.84	202.38	3.08
8	140.51	16.26	16.05	2.57	180.32	4.02
9	113.34	13.41	12.95	3.50	170.46	3.22
10	100.72	11.77	11.51	2.48	142.34	7.51

Table A12
Pressure integral results for wave 3.

Gauge ID	P_C , Pa s	U_{CT} , Pa s	U_{CD} , Pa s	U_{CP} , Pa s	P_E , Pa s	U_{ET} , Pa s
1	152.55	13.42	12.96	3.48	191.71	4.59
2	148.23	13.11	12.60	3.62	178.96	3.55
3	135.35	11.85	11.50	2.86	156.00	7.72
4	159.21	13.94	13.53	3.37	167.67	6.32
5	152.89	13.16	12.99	2.08	146.54	1.76
6	147.28	12.81	12.52	2.73	183.92	2.75
7	218.97	18.80	18.61	2.68	245.51	7.48
8	206.77	18.10	17.57	4.33	225.16	9.04
9	171.43	15.15	14.57	4.14	204.30	5.15
10	143.22	12.35	12.17	2.07	160.71	2.46

Table A13
Pressure integral results for wave 4.

Gauge ID	P_C , Pa s	U_{CT} , Pa s	U_{CD} , Pa s	U_{CP} , Pa s	P_E , Pa s	U_{ET} , Pa s
1	107.27	22.37	22.24	2.42	119.08	8.85
2	104.79	21.90	21.72	2.79	112.43	5.74
3	90.96	19.15	18.86	3.35	95.59	4.13
4	118.34	24.64	24.53	2.32	114.77	8.10
5	113.80	23.85	23.59	3.55	75.41	4.15
6	112.86	23.98	23.40	5.27	141.68	1.41
7	160.76	33.46	33.32	2.96	163.19	8.00

Table A13 (continued)

Gauge ID	P_C , Pa s	U_{CT} , Pa s	U_{CD} , Pa s	U_{CP} , Pa s	P_E , Pa s	U_{ET} , Pa s
8	141.36	29.42	29.30	2.59	112.17	11.15
9	122.60	26.17	25.41	6.26	117.99	9.41
10	110.28	23.22	22.86	4.10	106.96	2.80

Table A14

Pressure integral results for wave 5.

Gauge ID	P_C , Pa s	U_{CT} , Pa s	U_{CD} , Pa s	U_{CP} , Pa s	P_E , Pa s	U_{ET} , Pa s
1	138.80	6.37	6.11	1.80	127.59	17.02
2	139.27	6.52	6.13	2.21	120.27	17.11
3	125.99	5.93	5.55	2.09	118.51	15.49
4	148.84	6.99	6.55	2.44	157.94	10.25
5	143.80	7.00	6.33	2.98	137.86	3.08
6	137.18	6.95	6.04	3.44	135.83	2.31
7	243.18	11.91	10.70	5.22	294.40	5.99
8	224.98	10.54	9.90	3.61	217.40	3.54
9	178.82	8.71	7.87	3.72	211.75	2.82
10	130.81	6.45	5.76	2.90	130.15	20.70

Table A15

Pressure integral results for wave 6.

Gauge ID	P_C , Pa s	U_{CT} , Pa s	U_{CD} , Pa s	U_{CP} , Pa s	P_E , Pa s	U_{ET} , Pa s
1	192.48	30.88	30.75	2.82	168.38	19.74
2	182.24	29.32	29.12	3.43	163.53	19.25
3	156.74	25.33	25.04	3.78	140.47	6.80
4	197.39	32.31	31.54	7.01	193.44	13.82
5	192.70	31.58	30.79	7.04	232.45	19.51
6	185.06	29.98	29.57	4.94	198.40	16.85
7	361.07	58.04	57.69	6.41	415.91	10.43
8	332.94	53.78	53.19	7.94	332.86	12.63
9	262.31	42.14	41.91	4.40	327.00	6.18
10	155.51	26.09	24.85	7.95	134.95	2.99

Table A16

Pressure integral results for wave 7.

Gauge ID	P_C , Pa s	U_{CT} , Pa s	U_{CD} , Pa s	U_{CP} , Pa s	P_E , Pa s	U_{ET} , Pa s
1	158.47	3.27	0.51	3.23	234.89	11.51
2	154.73	2.53	0.50	2.48	222.80	8.79
3	140.76	2.93	0.45	2.90	210.26	12.02
4	183.33	3.91	0.59	3.87	279.12	21.62
5	182.57	2.32	0.59	2.24	303.16	6.69
6	169.02	4.19	0.54	4.16	272.94	6.48
7	304.56	6.80	0.98	6.73	529.92	8.32
8	266.56	3.89	0.86	3.79	427.49	6.72
9	222.36	2.44	0.71	2.33	366.28	4.14
10	158.95	2.69	0.51	2.64	194.10	3.80

Table A17

Pressure integral results for wave 8.

Gauge ID	P_C , Pa s	U_{CT} , Pa s	U_{CD} , Pa s	U_{CP} , Pa s	P_E , Pa s	U_{ET} , Pa s
1	263.23	5.78	0.07	5.78	322.13	18.72
2	242.58	7.85	0.07	7.85	329.91	13.27
3	221.99	5.70	0.06	5.70	276.22	15.84
4	311.79	4.72	0.08	4.72	397.30	26.77
5	305.47	3.80	0.08	3.80	411.73	9.18
6	279.10	3.64	0.08	3.64	410.62	7.44
7	508.78	11.36	0.14	11.36	693.53	23.35
8	455.81	7.82	0.12	7.82	551.77	13.61
9	378.50	5.88	0.10	5.88	479.35	8.50
10	250.51	3.85	0.07	3.85	278.32	5.50

Table A18
Pressure integral results for wave 9.

Gauge ID	P_C , Pa s	U_{CT} , Pa s	U_{CD} , Pa s	U_{CP} , Pa s	P_E , Pa s	U_{ET} , Pa s
1	347.14	8.97	6.50	6.18	412.80	13.40
2	339.30	9.75	6.35	7.40	422.13	15.10
3	302.76	8.63	5.67	6.51	377.98	19.25
4	452.83	10.91	8.48	6.87	511.01	26.72
5	443.78	10.25	8.31	6.00	523.13	16.85
6	406.69	9.61	7.61	5.87	508.34	9.43
7	727.35	19.11	13.62	13.41	843.18	16.82
8	632.93	14.63	11.85	8.59	690.75	26.37
9	522.18	13.17	9.77	8.83	585.76	14.96
10	378.33	9.45	7.08	6.25	360.47	18.52

References

- Eça, L., Hoekstra, M., 2008. Code verification of unsteady flow solvers with the method of the manufactured solutions. *Int. J. Offshore Polar Eng.* 18 (2).
- Eça, L., Hoekstra, M., 2014. A procedure for the estimation of the numerical uncertainty of CFD calculations based on grid refinement studies. *J. Comput. Phys.* 262, 104–130. <https://doi.org/10.1016/j.jcp.2014.01.006>.
- Greco, M., Lugni, C., 2012. 3-D seakeeping analysis with water on deck and slamming. Part 1: numerical solver. *J. Fluids Struct.* 33, 127–147. <https://doi.org/10.1016/j.jfluidstructs.2012.04.005>. GotoISI://WOS:000307413200008.
- Greco, M., Bouscasse, B., Lugni, C., 2012. 3-D seakeeping analysis with water on deck and slamming. Part 2: experiments and physical investigation. *J. Fluids Struct.* 33, 127–147. <https://doi.org/10.1016/j.jfluidstructs.2012.04.005>. GotoISI://WOS:000307413200008.
- Jasak, H., 1996. Error Analysis and Estimation for the Finite Volume Method with Applications to Fluid Flows. Ph.D. thesis. Imperial College of Science, Technology & Medicine, London.
- Jasak, H., 2009. OpenFOAM: open source CFD in research and industry. *Int. J. Nav. Archit. Ocean Eng.* 1 (2), 89–94.
- Jasak, H., Gatin, I., Vukčević, V., 2014. Numerical simulation of wave loading on static offshore structures. In: 11th World Congress on Computational Mechanics (WCCM XI), pp. 5151–5159.
- Jasak, H., Vukčević, V., Gatin, I., 2015. Numerical Simulation of Wave Loads on Static Offshore Structures, in: *CFD for Wind and Tidal Offshore Turbines*. Springer Tracts in Mechanical Engineering, pp. 95–105.
- Joga, R., Saripilli, J., Dhavalikar, S., Kar, A., 2014. Numerical simulations to compute rate of water ingress into open holds due to green waters. In: *Proceedings of the 24th International Offshore and Polar Engineering Conference ISOPE*, Busan, Korea.
- Kim, S., Kim, C., Cronin, D., 2013. Green water impact loads on breakwaters of large container carriers. In: *Proceedings of the 12th International Symposium on Practical Design of Ships and Other Floating Structures PRADS*, Changwon, Korea.
- Lee, H.-H., Lim, H.-J., Rhee, S.H., 2012. Experimental investigation of green water on deck for a CFD validation database. *Ocean. Eng.* 42, 47–60. <https://doi.org/10.1016/j.oceaneng.2011.12.026>.
- Lu, H., Yang, C., Loehner, R., 2012. Numerical Studies of Green Water Impact on Fixed and Moving Bodies. *International Society of Offshore and Polar Engineers*, p. 22.
- Pakozdi, C., Östman, A., Stansberg, C., Carvalho, D., 2014. Green water on FPSO analyzed by a coupled Potential-Flow-NS-VOF method. In: *Proceedings of the 33rd International Conference on Ocean, Offshore and Arctic Engineering OMAE*, San Francisco, USA.
- Rienecker, M.M., Fenton, J.D., 1981. A Fourier approximation method for steady water waves. *J. Fluid Mech.* 104, 119–137.
- Roenby, J., Bredmose, H., Jasak, H., 2016. A computational method for sharp interface advection. *Open Sci.* 3 (11) <https://doi.org/10.1098/rsos.160405>.
- Ruggeri, F., Wata, R., Brisson, H., Mello, P., Sampaio Carvalho e Silva, C., Vieira, D., 2013. Numerical prediction of green water events in beam seas. In: *Proceedings of the 12th International Symposium on Practical Design of Ships and Other Floating Structures PRADS*, Changwon, Korea.
- Rusche, H., 2002. Computational Fluid Dynamics of Dispersed Two - Phase Flows at High Phase Fractions. Ph.D. thesis. Imperial College of Science, Technology & Medicine, London.
- Temarel, P., Bai, W., Bruns, A., Derbanne, Q., Dessi, D., Dhavalikar, S., Fonseca, N., Fukasawa, T., Gu, X., Nestegard, A., Papanikolaou, A., Parunov, J., Song, K.H., Wang, S., 2016. Prediction of wave-induced loads on ships: progress and challenges. *Ocean. Eng.* 119, 274–308.
- Vukčević, V., 2016. Numerical Modelling of Coupled Potential and Viscous Flow for Marine Applications. Ph.D. thesis. Faculty of Mechanical Engineering and Naval Architecture, University of Zagreb.
- Vukčević, V., Jasak, H., Malenica, S., 2015. Assessment of higher-order forces on a vertical cylinder with decomposition model based on swense method. In: *Numerical Towing Tank Symposium*.
- Vukčević, V., Jasak, H., Gatin, I., Malenica, S., 2016. Seakeeping sensitivity studies using the decomposition CFD model based on the Ghost fluid method. In: *Proceedings of the 31st Symposium on Naval Hydrodynamics*.
- Vukčević, V., Jasak, H., Gatin, I., 2017. Implementation of the Ghost fluid method for free surface flows in polyhedral finite volume framework. *Comput. Fluids* 153, 1–19.
- Weller, H.G., Tabor, G., Jasak, H., Fureby, C., 1998. A tensorial approach to computational continuum mechanics using object oriented techniques. *Comput. Phys.* 12, 620–631.
- Xu, H., 2013. Numerical Simulation of Breaking Wave Impact on the Structure. Ph.D. thesis. National University of Singapore, Singapore (.
- Zhao, X., Ye, Z., Fu, Y., 2014. Green water loading on a floating structure with degree of freedom effects. *J. Mar. Sci. Technol.* 19, 302–313. <https://doi.org/10.1007/s00773-013-0249-7>.
- Zhu, R.C., Miao, G.P., Lin, Z.W., 2009. Numerical research on FPSOs with green water occurrence. *J. Ship Res.* 53 (1), 7–18. GotoISI://WOS:000265900000002.